Supporting Information for "*SASSY21*: A 3-D seismic structural model of the lithosphere and underlying mantle beneath Southeast Asia from multi-scale adjoint waveform tomography"

Deborah Wehner[1], Nienke Blom[1], Nicholas Rawlinson [1], Daryono[2], Christian Böhm[3,4], Meghan S. Miller[5], Pepen Supendi[2], and Sri Widiyantoro[6,7]

[1]Bullard Laboratories, Department of Earth Sciences, University of Cambridge, Cambridge, UK

[2]Indonesian Agency for Meteorology, Climatology, and Geophysics (BMKG)

[3]ETH Zürich, Zurich, Switzerland

[4]Mondaic AG, Zurich, Switzerland

[5]Australian National University, Canberra, Australia

[6]Global Geophysics Research Group, Faculty of Mining and Petroleum Engineering, Institut Teknologi Bandung, Bandung, Indonesia

[7]Faculty of Engineering, Maranatha Christian University, Bandung, Indonesia

Contents of this file

1. S1 presents the starting model.

2. Table S2.1 contains an overview of the events used in this study. S2.2 shows the event misfit reduction for the final model relative to the starting model.

3. S3 provides a description and map of the station availability.

4. S4 gives more detail on the preconditioning steps applied to the gradients.

5. S5 elaborates further on technical details not described in the main text.

6. S6 presents further waveform fits.

7. S7 presents depth slices from 50 to 700 km for all inversion parameters (v_{SH}, v_{SV}, v_P and density).

Additional supporting information (files uploaded separately)

The final model is provided as *NetCDF* and *HDF5* files, with the former being readable by e.g. *xarray* (Hoyer & Hamman, 2017) and the latter suitable for viewing with *ParaView* (Ahrens et al., 2005) and interaction with *Salvus*. We further provide *SASSY21* in *CSV* format, and a Jupyter Notebook (Kluyver et al., 2016) demonstrating how to interact with the different file formats.

Introduction

In this Supplementary Material, we present the starting model (Section S1), provide additional detail about the earthquake data used throughout the inversion (Section S2.1), event misfits compared to hypocentral depth, magnitude and focal mechanism (Section S2.2), the stations used throughout this study (Section 3), the processing steps applied to the raw gradients (Section S4) and an overview of further technical parameters (Section 5). We also show further waveform fits in Section 6 and extra depth slices for v_{SV}, v_{SH}, v_P and density ρ (Section 7). The final model is provided separate to this document.

S1 Starting model

Figure S1 presents the absolute values of the 1-D starting model, which was taken from *CSEM* (Fichtner et al., 2018).

S2.1 Event overview

Table S2 contains an overview of the events used in this study. Event locations and moment tensors are retrieved from the *GCMT* catalog and remain constant throughout the inversion. The source time function is approximated by a Butterworth bandpass filtered Heaviside step function, representing an instantaneous rupture process. 15 events with depths > 300 km were selected to ensure a diversity of data coverage.

Table S2: List of events used throughout this study. The period bands used for each event are indicated by roman numerals in the last column, following the notation from Table S5. The first 50 events are used across all period bands.

#	Focaltime	M_w	Longitude	Latitude	Depth [km]	Period bands
1	2014-09-10T02:46:11.7	6.27	125.06	-0.36	29.2	I - VII
2	2014-12-02T05:11:37.2	6.58	123.17	6.31	631.7	I - VII
3	2014-12-06T22:05:14.8	6.04	130.57	-6.12	137.8	I - VII
4	2015-02-27T13:45:08.9	6.97	122.50	-7.35	551.5	I - VII
5	2015-03-03T10:37:35.7	6.18	98.58	-0.72	23.6	I - VII
6	2015-03-17T22:12:32.1	6.28	126.48	1.78	41.9	I - VII
7	2015-03-28T22:28:52.4	5.92	122.00	0.43	130.6	I - VII
8	2015-05-15T20:26:58.3	6.04	102.14	-2.61	158.4	I - VII
9	2015-07-03T06:43:24.4	6.11	126.25	10.08	43.8	I - VII
10	2015-07-26T07:05:09.9	5.90	112.82	-9.45	43.7	I - VII
11	2015-08-20T11:00:11.3	5.81	126.50	0.63	71.7	I - VII
12	2015-09-16T07:41:02.6	6.32	126.47	2.01	33.0	I - VII
13	2015-11-11T23:36:22.0	5.84	128.93	-7.41	137.0	I - VII
14	2015-11-21T09:06:16.2	6.04	130.11	-7.22	100.4	I - VII
15	2015-12-24T23:10:59.7	5.81	129.11	-7.34	132.1	I - VII
16	2016-01-11T16:38:11.6	6.49	127.05	3.84	12.0	I - VII
17	2016-02-12T10:02:29.4	6.24	119.35	-9.87	38.0	I - VII
18	2016-04-05T08:29:39.2	5.92	126.63	4.21	29.7	I - VII
19	2016-04-06T14:45:35.3	6.05	107.42	-8.41	41.9	I - VII
20	2016-06-05T16:25:36.5	6.30	125.56	-4.51	449.0	I - VII
21	2016-09-04T02:38:13.9	5.77	125.85	8.38	19.0	I - VII
22	2016-09-23T22:53:11.3	6.30	126.49	6.55	63.2	I - VII

Continued on next page

Table S2 – *Continued from previous page*

#	Focaltime	M_w	Longitude	Latitude	Depth [km]	Period bands
23	2016-10-19T00:26:04.8	6.61	108.07	-4.95	622.8	I - VII
24	2016-10-27T08:17:52.2	5.78	125.88	1.40	67.8	I - VII
25	2016-12-05T01:13:07.2	6.28	123.46	-7.36	531.9	I - VII
26	2016-12-29T22:30:21.9	6.26	118.74	-9.16	98.4	I - VII
27	2017-04-28T20:23:23.6	6.85	124.89	5.49	31.4	I - VII
28	2017-07-15T12:12:22.5	5.94	121.95	0.44	125.8	I - VII
29	2017-08-13T03:08:17.8	6.47	101.43	-3.81	43.3	I - VII
30	2017-12-15T16:48:00.7	6.55	108.11	-7.91	109.4	I - VII
31	2018-01-23T06:34:57.0	6.02	106.16	-7.18	53.1	I - VII
32	2018-02-26T13:34:58.8	6.00	126.82	-2.65	12.9	I - VII
33	2018-03-02T02:20:14.5	5.93	130.35	-6.17	151.9	I - VII
34	2018-03-25T20:14:50.2	6.43	129.84	-6.72	181.7	I - VII
35	2018-04-05T03:53:42.0	6.06	126.88	6.69	45.5	I - VII
36	2018-05-10T18:02:29.8	5.88	123.70	6.95	543.1	I - VII
37	2018-08-17T15:35:04.1	6.51	119.75	-7.31	538.9	I - VII
38	2018-11-04T07:55:29.9	5.99	123.75	7.82	599.3	I - VII
39	2018-12-01T13:27:25.2	6.47	128.67	-7.47	146.0	I - VII
40	2018-12-29T03:39:14.8	6.98	126.91	5.87	54.4	I - VII
41	2019-02-08T11:55:12.6	5.90	126.41	9.85	20.8	I - VII
42	2019-03-06T00:13:04.8	5.86	127.05	8.49	18.1	I - VII
43	2019-03-08T15:06:16.4	6.06	126.20	10.35	43.3	I - VII
44	2019-04-06T21:55:04.1	6.28	124.86	-6.92	546.5	I - VII
45	2019-05-31T10:12:33.1	6.15	126.54	6.22	87.9	I - VII
46	2019-08-02T12:03:34.8	6.89	104.85	-7.40	51.9	I - VII
47	2019-09-21T19:53:15.4	5.88	130.50	-6.46	87.8	I - VII
48	2019-09-29T02:02:53.4	6.25	126.58	5.65	77.3	I - VII
49	2019-10-29T01:04:49.0	6.61	125.05	6.87	18.0	I - VII
50	2020-04-05T18:37:14.9	6.02	126.33	1.53	41.3	I - VII
51	2014-09-10T05:16:56.8	5.89	125.12	-0.33	26.5	I - III
52	2014-11-26T14:33:50.0	6.77	126.44	2.11	35.2	I - III
53	2014-11-29T19:40:15.3	5.77	126.99	2.51	27.4	I - III
54	2014-12-29T09:29:40.9	6.14	121.45	8.68	15.0	I - III
55	2015-03-15T23:17:28.2	6.06	122.35	-0.53	25.1	I - III
56	2015-11-04T03:44:21.2	6.54	124.95	-8.20	12.0	I - III
57	2015-12-09T10:21:54.6	6.79	129.51	-4.16	12.2	I - III
58	2016-06-07T19:15:19.5	6.36	126.35	1.41	31.4	I - III
59	2017-02-10T14:03:47.5	6.47	125.49	9.85	12.0	I - III
60	2018-08-05T11:46:44.7	6.94	116.24	-8.33	17.8	I - III
61	2018-09-08T07:16:52.7	6.13	126.43	7.14	15.1	I - III
62	2018-09-28T10:02:59.4	7.57	119.86	-0.72	12.0	I - III
63	2018-10-10T18:44:59.0	5.97	114.48	-7.45	13.5	I - III
64	2018-12-28T03:03:35.5	5.81	134.01	-1.41	48.8	I - III
65	2019-07-14T09:11:04.6	7.19	128.13	-0.72	12.0	I - III

Continued on next page

Table S2 – *Continued from previous page*

#	Focaltime	M_w	Longitude	Latitude	Depth [km]	Period bands
66	2020-01-19T16:58:22.9	6.19	123.87	-0.15	129.4	I - III
67	2014-01-25T05:14:22.8	6.15	109.27	-8.36	76.1	I - IV
68	2014-11-21T10:10:25.4	6.54	127.08	2.60	30.1	I - IV
69	2014-12-17T06:10:10.0	5.79	99.84	-4.04	14.9	I - IV
70	2015-06-04T23:15:46.6	5.99	116.65	6.17	12.3	I - IV
71	2015-06-15T17:41:00.1	5.81	125.12	-9.62	18.6	I - IV
72	2017-11-18T16:07:05.0	5.81	128.10	2.59	14.1	I - IV
73	2018-08-09T05:25:34.9	5.91	116.20	-8.38	21.9	I - IV
74	2018-10-01T23:59:47.5	5.97	120.16	-10.57	22.0	I - IV
75	2019-07-08T18:52:38.1	5.88	126.38	0.35	19.6	I - IV
76	2019-10-14T22:23:59.9	6.08	101.04	-4.57	12.0	I - IV
77	2014-05-15T10:16:47.5	6.25	121.92	9.40	24.0	I - V
78	2014-08-06T11:45:28.7	6.19	127.92	-7.13	19.5	I - V
79	2015-09-24T15:53:33.7	6.58	131.23	-0.62	18.9	I - V
80	2015-12-20T18:47:38.1	6.05	117.56	3.66	12.0	I - V
81	2016-02-17T17:26:05.0	6.09	128.98	0.84	15.5	I - V
82	2016-06-09T04:13:11.2	6.06	116.29	-11.30	31.5	I - V
83	2016-10-09T14:46:28.1	5.82	127.48	1.82	141.1	I - V
84	2016-11-07T21:31:30.5	5.78	104.83	-8.32	41.8	I - V
85	2016-12-06T22:03:39.5	6.56	96.22	5.28	17.5	I - V
86	2017-04-11T21:21:01.5	5.83	124.70	7.74	12.0	I - V
87	2017-07-06T08:04:00.6	6.48	124.68	11.15	12.0	I - V
88	2017-07-10T01:41:52.6	5.80	124.76	11.08	13.6	I - V
89	2017-07-27T12:08:41.9	5.78	125.89	-3.52	20.7	I - V
90	2018-04-15T19:30:47.4	6.02	126.85	1.51	40.2	I - V
91	2018-08-19T14:56:35.6	6.93	116.75	-8.40	23.5	I - V
92	2018-08-28T07:08:17.9	6.18	124.14	-10.82	12.0	I - V
93	2018-10-02T00:16:48.8	5.92	120.07	-10.53	24.4	I - V
94	2019-01-21T23:59:28.3	6.09	119.09	-10.32	20.4	I - V
95	2019-01-22T05:10:09.4	6.44	119.07	-10.37	19.4	I - V
96	2019-07-07T15:08:47.3	6.91	126.10	0.55	30.5	I - V
97	2019-07-12T20:42:58.5	5.79	125.94	9.35	12.0	I - V
98	2019-09-14T16:21:32.2	5.86	128.57	-0.94	12.0	I - V
99	2019-09-25T23:46:48.4	6.47	128.39	-3.54	12.7	I - V
100	2019-10-16T11:37:10.3	6.42	125.01	6.86	17.1	I - V
101	2019-10-31T01:11:21.4	6.47	125.10	6.98	12.0	I - V
102	2019-11-15T01:17:43.0	5.98	126.25	1.69	28.8	I - V
103	2019-11-16T10:19:19.5	5.86	126.16	1.80	27.3	I - V
104	2019-11-18T13:22:12.8	5.90	124.87	7.69	1	I - V
105	2019-12-15T06:11:57.1	6.74	125.14	6.72	12.0	I - V
106	2020-01-07T06:05:24.9	6.34	96.27	2.21	12.0	I - V
107	2020-03-18T17:45:43.8	6.25	115.10	-11.23	12.0	I - V
108	2020-03-28T15:43:20.2	5.84	120.18	-1.68	18.9	I - V

Continued on next page

Table S2 – *Continued from previous page*

#	Focaltime	M_w	Longitude	Latitude	Depth [km]	Period bands
109	2014-02-03T22:36:42.4	5.87	128.20	-7.12	12.0	I - VI
110	2014-05-01T14:35:42.3	5.85	97.72	1.88	43.5	I - VI
111	2014-11-15T02:31:49.8	7.05	126.37	1.98	38.1	I - VI
112	2014-12-21T11:34:18.3	6.39	126.51	2.29	33.4	I - VI
113	2016-06-01T22:56:05.0	6.67	100.57	-2.18	28.9	I - VI
114	2017-01-10T06:13:55.9	7.27	122.78	4.57	621.5	I - VI
115	2017-05-29T14:35:28.3	6.58	120.40	-1.24	12.0	I - VI
116	2017-10-31T11:50:52.4	6.10	127.71	-3.83	12.0	I - VI
117	2019-01-06T17:27:24.2	6.63	126.63	2.48	34.9	I - VI
118	2019-07-01T16:59:26.1	5.93	124.09	9.15	545.8	I - VI
119	2014-04-17T04:38:20.0	5.76	122.82	4.55	575.0	IV
120	2018-03-08T13:06:14.5	5.53	116.65	6.15	12.0	IV, V
121	2018-08-25T18:33:18.7	5.54	116.99	-8.48	12.0	IV - VI
122	2014-10-30T12:11:36.8	5.76	117.48	-6.94	547.4	IV - VII
123	2016-03-19T08:51:26.5	5.70	129.43	-5.56	282.0	IV - VII
124	2016-04-15T04:50:12.9	5.59	126.98	2.06	108.7	IV - VII
125	2016-11-16T15:10:13.1	5.71	113.18	-9.14	105.7	IV - VII
126	2016-11-17T16:56:46.3	5.57	130.48	-6.33	127.5	IV - VII
127	2016-12-04T05:24:08.2	5.73	127.86	4.52	161.6	IV - VII
128	2017-03-21T23:10:28.1	5.69	115.27	-8.75	130.2	IV - VII
129	2018-03-25T08:58:12.6	5.73	128.50	-7.40	160.1	IV - VII
130	2018-12-03T14:00:09.3	5.54	128.72	-7.52	142.9	IV - VII
131	2018-12-30T08:39:14.2	5.80	102.25	-2.68	175.5	IV - VII
132	2019-07-16T00:18:38.3	5.78	114.50	-9.01	102.7	IV - VII
133	2020-02-05T18:12:36.8	6.23	113.09	-6.11	597.0	IV - VII
134	2017-12-28T17:20:23.4	5.75	126.83	4.10	32.5	VI
135	2008-09-11T00:00:06.8	6.58	127.34	1.91	119.6	VI, VII
136	2015-02-25T01:31:44.7	5.67	119.87	6.15	18.4	VI, VII
137	2016-04-13T18:21:55.9	5.97	121.94	7.84	24.2	VI, VII
138	2017-05-20T01:06:16.4	5.98	124.02	9.33	544.6	VI, VII
139	2018-02-02T00:20:43.6	5.60	125.13	-0.32	30.9	VI, VII
140	2018-06-02T16:29:03.2	5.80	126.76	4.59	28.2	VI, VII
141	2019-02-07T04:15:33.3	5.72	126.39	1.53	40.5	VI, VII
142	2019-03-24T04:37:39.1	6.15	126.36	1.77	41.9	VI, VII
143	2019-06-14T20:10:55.2	5.71	130.77	-5.80	129.2	VI, VII

S2.2 Event misfits

In Figure S2.1, we show the event misfit reduction for the final model relative to the starting model, normalized to the total misfit decrease. No single event contributes more

than 3 % to the total misfit decrease, indicating that the inversion is not driven by data from only a small subset of events. Furthermore, no patterns associated with a dependency on focal mechanisms or hypocentral depths are identifiable.

S3 Station availability

Figure S3 presents a map of all 440 stations used in this study. Publicly available waveforms including instrument responses were downloaded automatically using *obspyDMT* (Hosseini & Sigloch, 2017), which accesses over 20 data centers via the *International Federation of Digital Seismograph Networks (FDSN)* and *ArcLink* interfaces. To date, only a small proportion of permanent network stations have their data made publicly accessible within the region. Thus, the majority of our dataset consists of stations from several networks with restricted access:

- *IA*, accessed via the *Badan Meteorologi, Klimatologi, dan Geofisika (BMKG) WebDC3* web interface (Bianchi et al., 2015)
- Most of the *MY* network
- *YC* (Rawlinson, 2018)
- *YS* (Miller, 2014) accessed via the *Australian Passive Seismic Server (AusPass) WebDC3* web interface (Bianchi et al., 2015)
- *9G* (Greenfield, 2018)

Data from a Taiwanese station in the South China Sea (*TW.VNAS*) is recorded as part of the *Broadband Array in Taiwan for Seismology (BATS)*, and was requested from the *Academia Sinica, Institute of Earth Sciences* in Taipei since it is publicly available only

before 2014. More information about individual networks can be found here: `https://www.fdsn.org/networks/`.

S4 Gradient preconditioning

Event kernels usually show large sensitivities around the source region, with values typically around five times higher than the surrounding region in this study. Thus, these imprints have to be removed to avoid a strong localization of model updates (see Figure S4a). We favor not applying the source imprint removal to the summed gradient, but to the event kernels individually, otherwise the gradient will turn into a "Swiss cheese" and constraint around *all* event hypocentres is lost. The removal region is defined by a sphere with the radii for the source imprint removal shown in Table 1, and a radius of 50 km for each receiver. However, receiver imprints are smaller and usually wiped out by the smoothing operator described in the next section.

Initial model updates (100 – 65 s) use an anisotropic smoothing operator (horizontal and vertical smoothing lengths are fixed across the model). From 50 s onwards, depth-dependent smoothing is applied in order to account for the local wavelengths of the model. The respective wavelengths are based on the shear wave velocity of the prior model. The effect of the smoothing operator is presented in Figure S4b.

S5 Technical details

In Table S5, an overview of the technical parameters is given. Throughout the entire inversion, 1.5 elements per minimum wavelength are used and velocity seismograms are considered. Note that each period decrease is accompanied by a decrease in the smoothing lengths since the smoothing operator is based on the minimum wavelength considered.

The simulation time is decreased since the surface wave train becomes more compact, which spares computational resources.

To account for the remaining non-physical boundaries of the computational domain, a first order Clayton-Enquist boundary condition (Clayton & Engquist, 1977) is applied and the 3-D wavefield is attenuated within absorbing boundary layers following Kosloff and Kosloff (1986). The absorbing layer width is based on 3.5 minimum wavelengths at a reference velocity of 6 km/s.

S6 Waveform fits

Figure S6 shows additional three-component waveform fits not shown in the main text.

S7 Depth slices

Figures S7a – S7d present depth slices from 50 to 700 km for all inversion parameters (v_{SV}, v_{SH}, v_P and ρ).

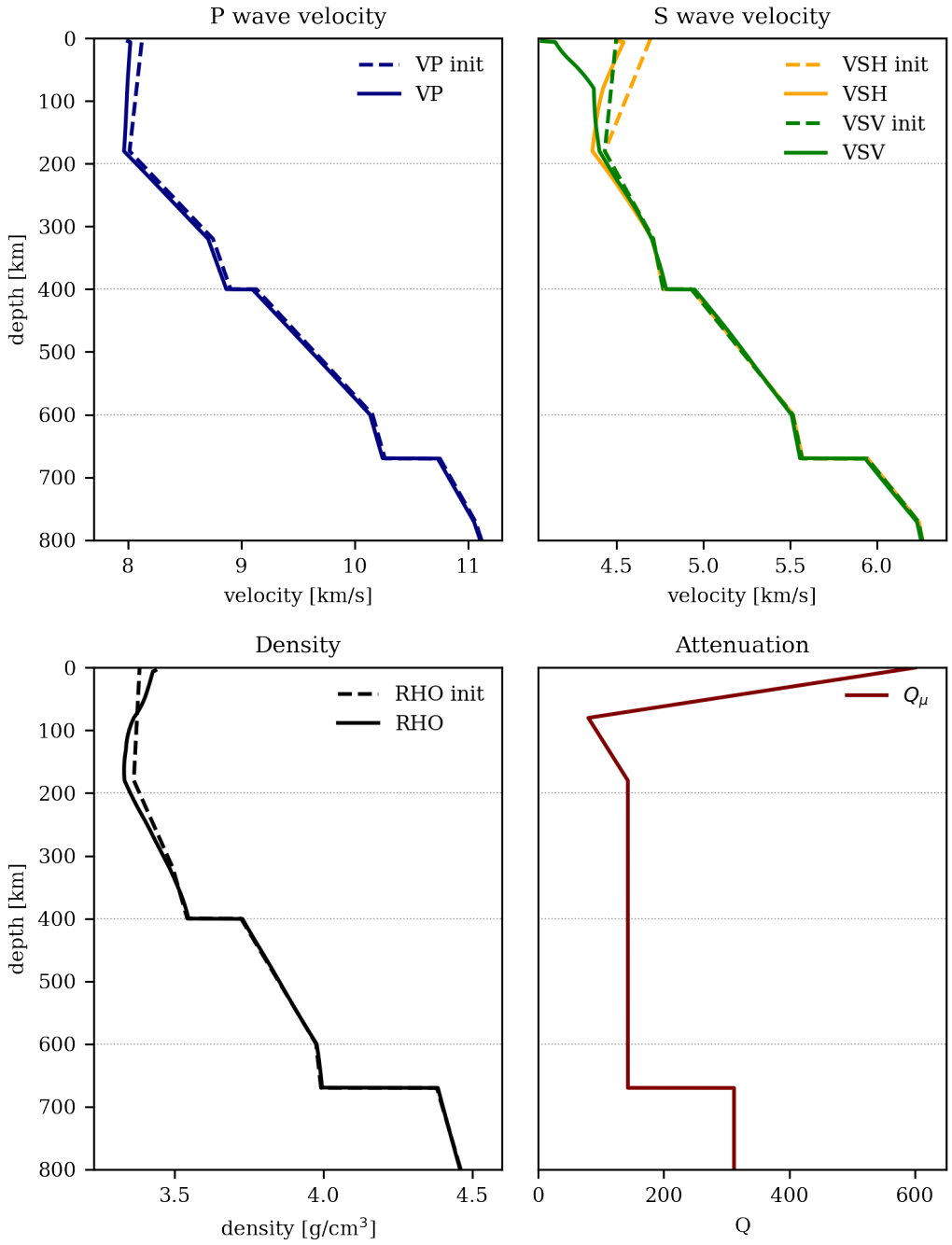

Figure S1. Absolute values for the starting model (dashed lines) and final model (solid lines) for the upper 800 km, which is equivalent to the mesh depth in this study (without absorbing layers). Q_μ and Q_κ remain constant throughout the inversion. Q_κ is not shown, but has a constant value of 57,823.

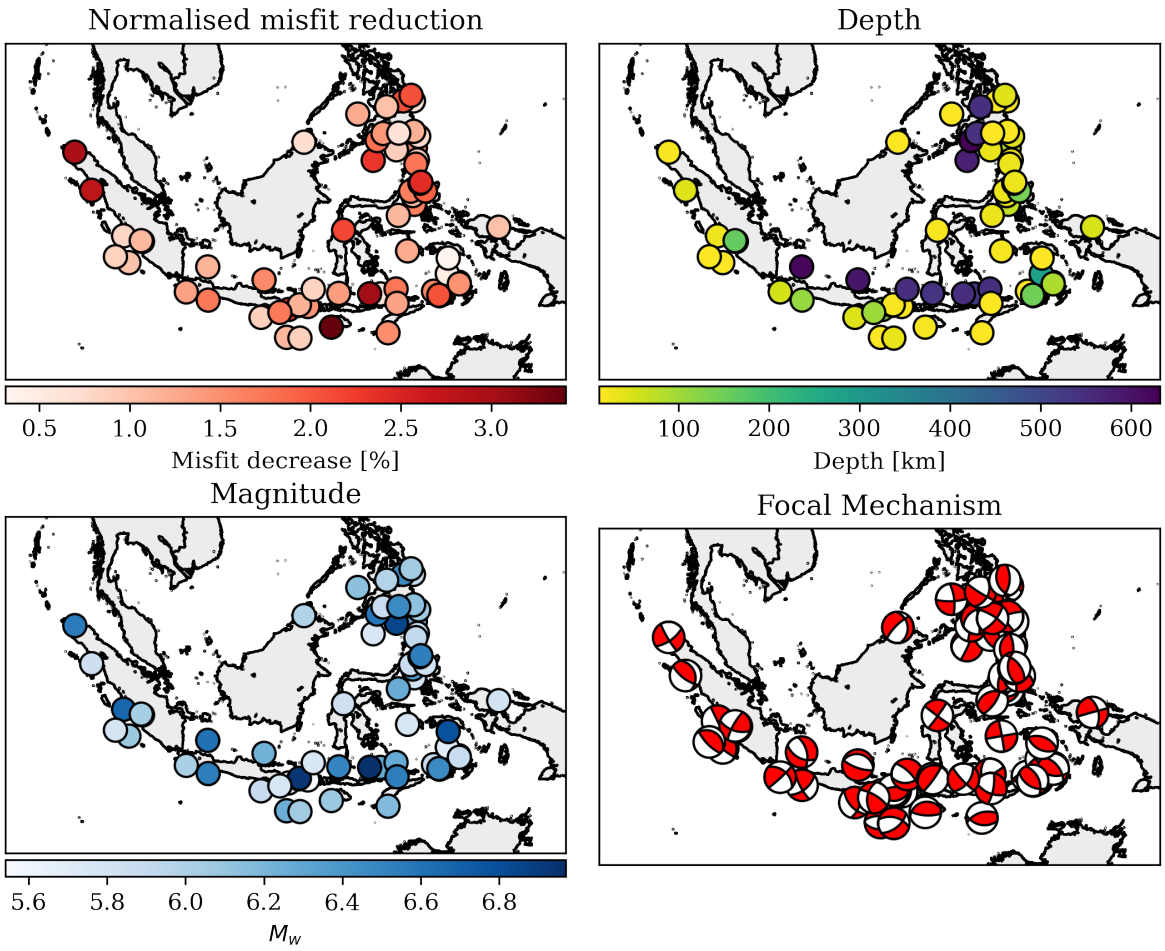

Figure S2.1. *Top left:* The normalized event misfit reduction for each event. *Top right:* Events colored by depth. *Bottom left:* Events colored by magnitude. *Bottom right:* Focal mechanisms.

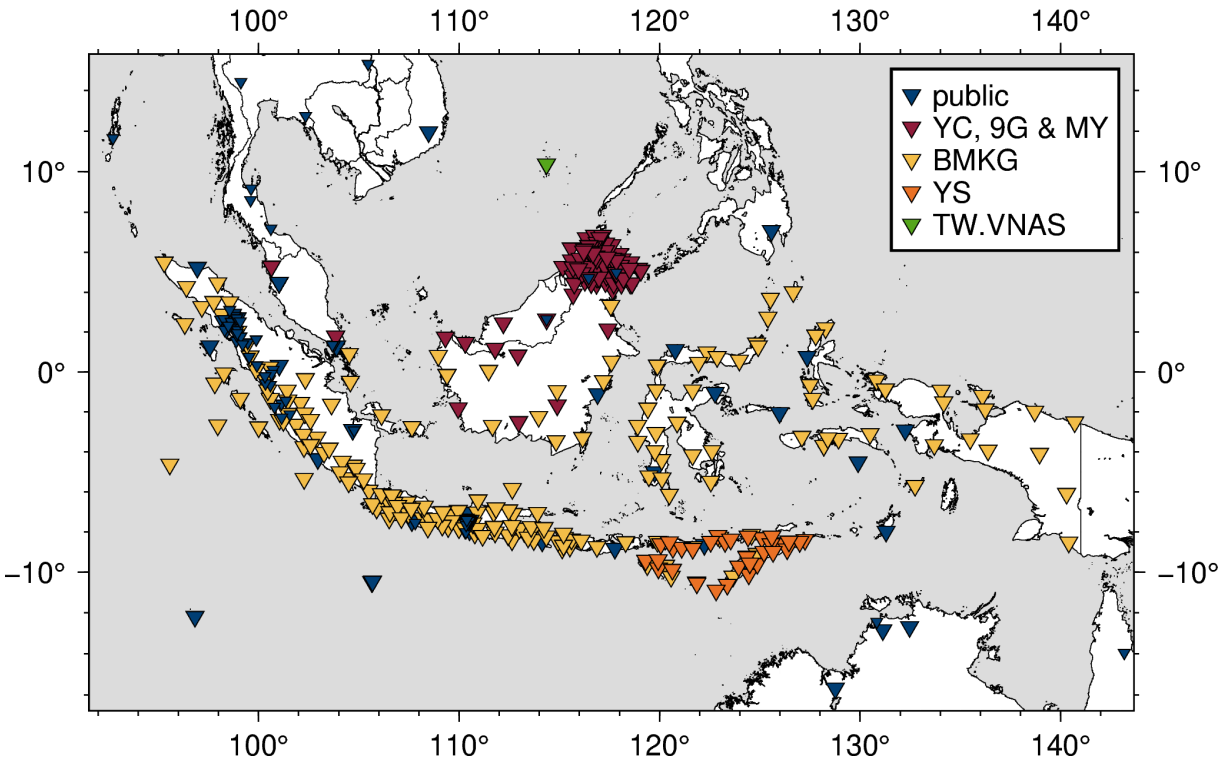

Figure S3. Map showing the 440 on-shore stations used in this study. Publicly available stations are shown in blue. Public stations contributing < 30 waveforms to the inversion are plotted in smaller size, e.g. temporary networks on Java and Sumatra.

Table S4. Overview of the smoothing lengths chosen throughout this study. During the initial period bands (100 – 65 s), a purely anisotropic, diffusion-based smoothing (PA) is applied. From 50 s onwards, a depth-dependent, anisotropic, diffusion-based smoothing (DD) is used.

period band	**smoothing type**	**smoothing lengths – horizontal, vertical**	**source imprint removal [km]**
100 s (Ia)	PA	450, 100 km	500
100 s (Ib)	PA	375, 100 km	500
80 s (IIa)	PA	375, 80 km	450
80 s (IIb)	PA	300, 80 km	450
65 s (III)	PA	300, 65 km	400
50 s (IVa)	DD	1.0, 0.2 $\lambda_{\min}$	350
50 s (IVb)	DD	0.75, 0.2 $\lambda_{\min}$	350
40 s (V)	DD	0.5, 0.2 $\lambda_{\min}$	300
30 s (VI)	DD	0.5, 0.2 $\lambda_{\min}$	300
20 s (VII)	DD	0.5, 0.2 $\lambda_{\min}$	300

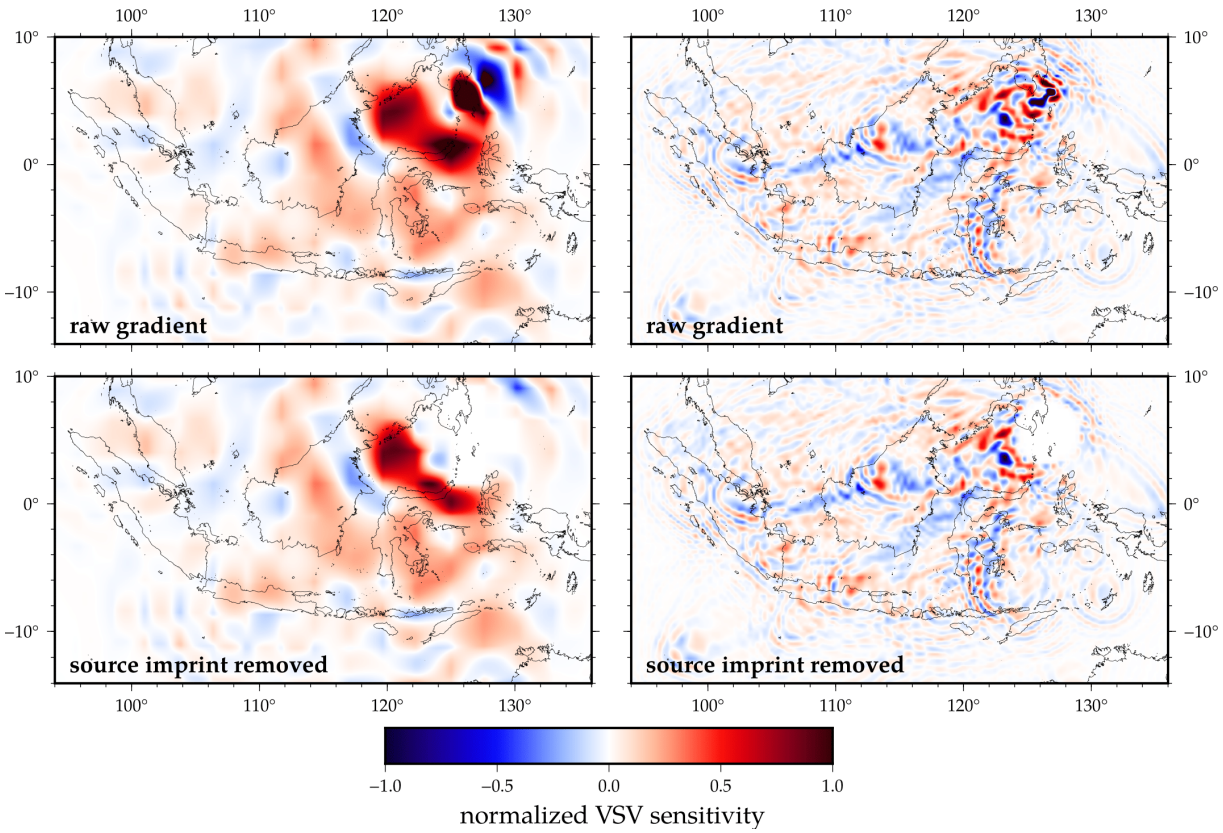

Figure S4a. Source imprint removal for a M_w6.3 event southeast of the Philippines at 100 s (left column, iteration 5) and 20 s (right column, iteration 87) for a depth slice at 75 km, which is the event's hypocentral depth taken from *GCMT*. The upper row shows the raw v_{SV} event kernel, and the bottom row shows the event kernel after the source imprints have been removed. Note the radius decrease of the source imprint removal and the overall smaller scale structure as we consider shorter periods. The sensitivities are normalized per period band since the gradients of 100 and 20 s vary by two orders of magnitude. The receiver imprints have not yet been removed.

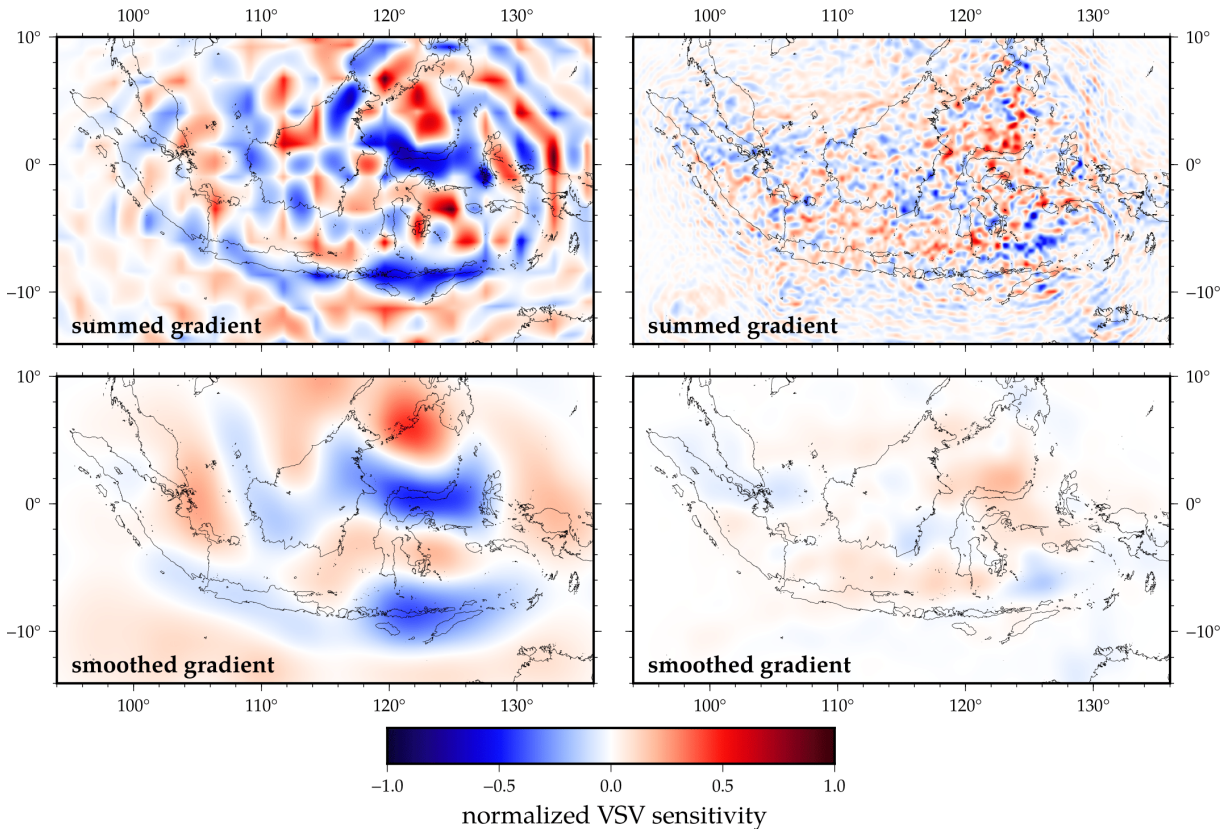

Figure S4b. Smoothing of the misfit gradient, at 100 s (left column, iteration 5) and 20 s (right column, iteration 87) for a depth slice at 75 km. The upper row shows the summed v_{SV} gradient after the source imprint has been removed, and the bottom row shows the smoothed gradient. The sensitivities are normalized per period band since the gradients of 100 and 20 s vary by two orders of magnitude. Note the sensitivity to smaller scale structure as the period is decreased.

Table S5. Overview of technical parameters.

period band	# iterations	# mesh elements	absorbing layer width [km]	simulation time [s]	time step [s]
100 s (Ia)	0 - 5	14,250	2,100	1,600	0.55
100 s (Ib)	5 - 8	14,250	2,100	1,600	0.55
80 s (IIa)	8 - 15	17,600	1,680	1,600	0.55
80 s (IIb)	15 - 19	17,600	1,680	1,600	0.55
65 s (III)	19 - 27	23,400	1,365	1,600	0.55
50 s (IVa)	27 - 32	33,866	1,050	1,600	0.5
50 s (IVb)	32 - 46	33,866	1,050	1,600	0.5
40 s (V)	46 - 57	49,680	840	1,500	0.45
30 s (VI)	57 - 70	84,796	630	1,250	0.375
20 s (VII)	70 - 87	207,636	420	1,100	0.28

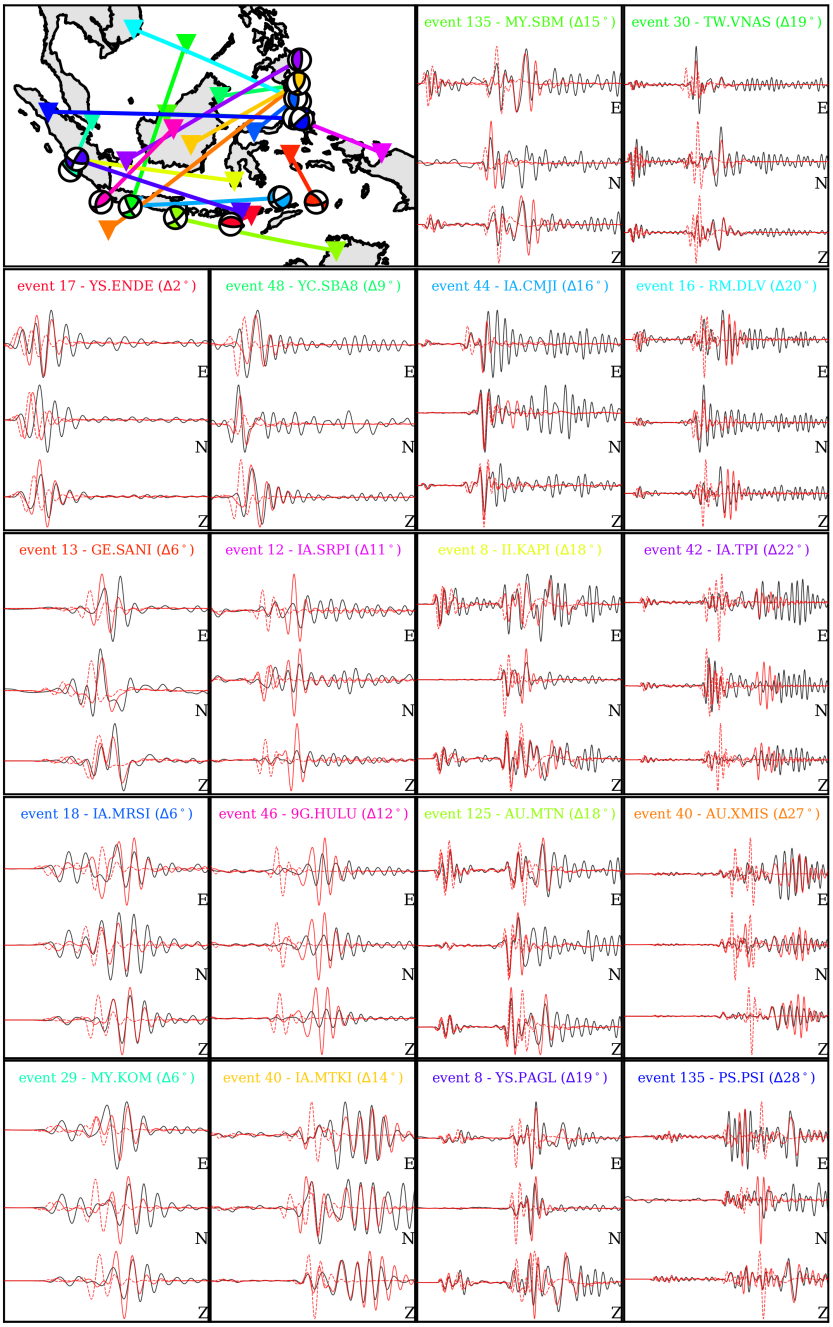

Figure S6. Three-component waveform match for the initial model (iteration 0, dashed red), the final synthetics (iteration 87, solid red) and observed waveforms (black) for 18 source-receiver pairs. The event numbers are taken from Table S2.

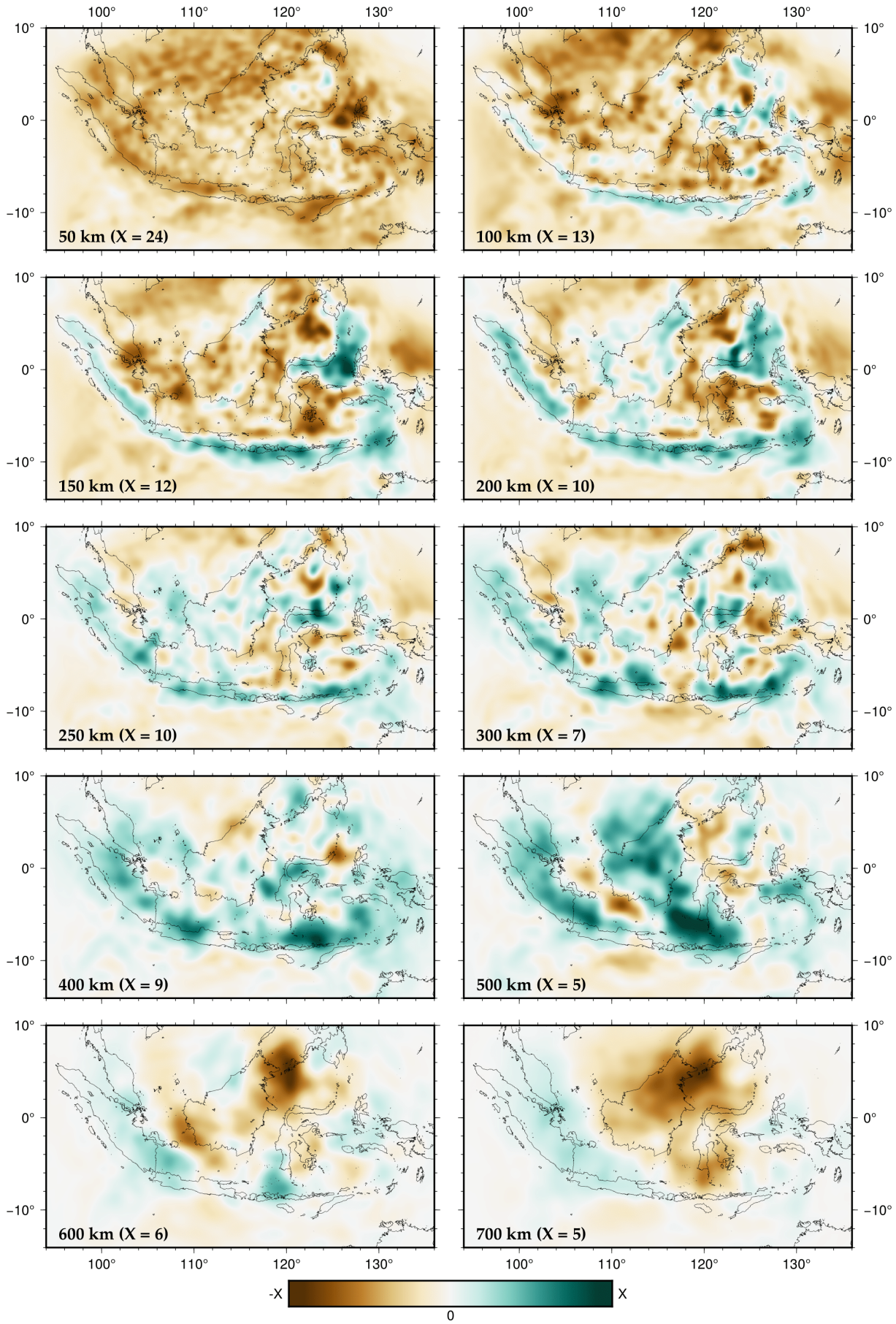

Figure S7a. v_{SV} depth slices from August 13, 2021, 5:40pm. Perturbations are in % relative to the initial model. The limits of the colorscale X are shown in the lower left corner of each plot.

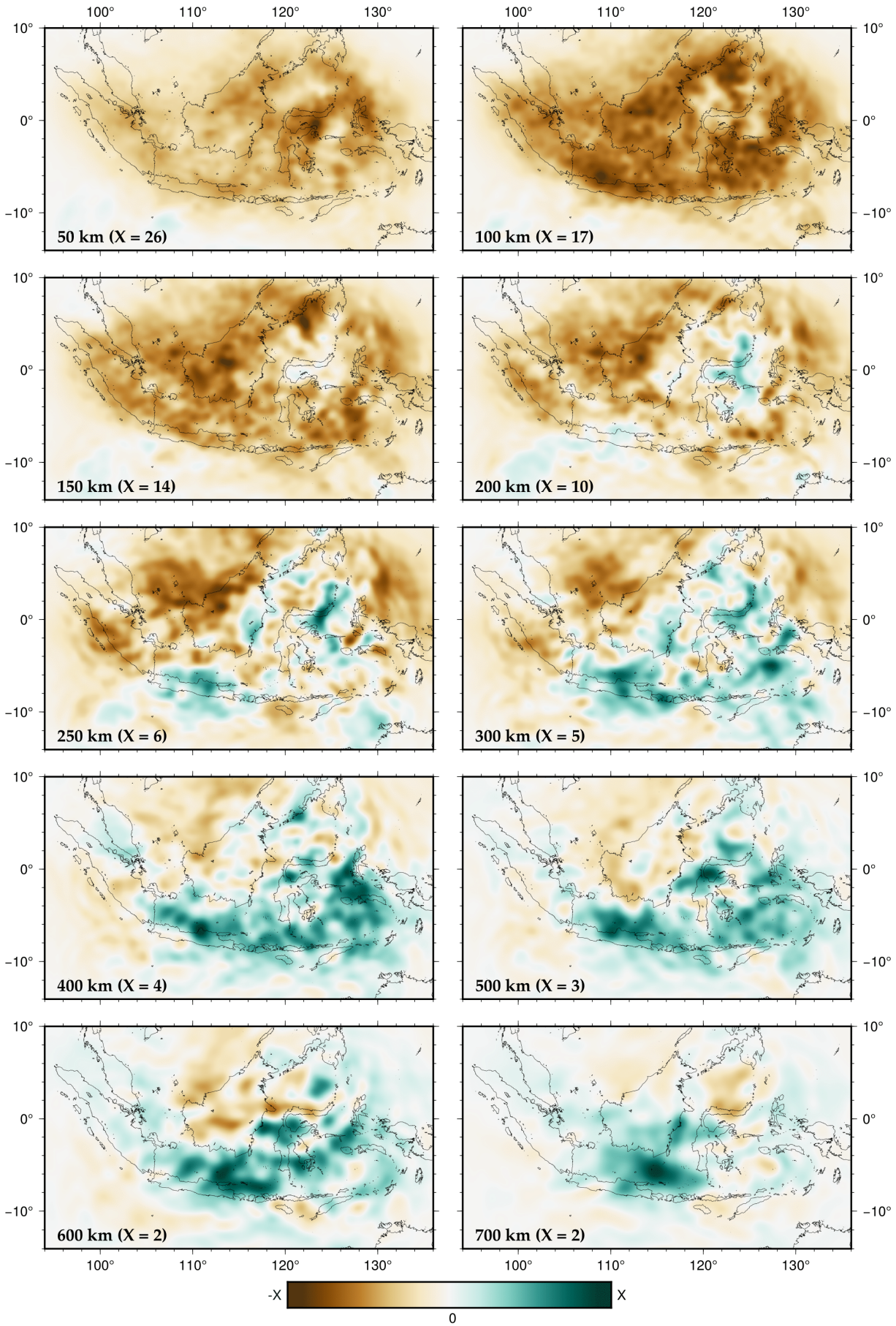

Figure S7b. v_{SH} depth slices from August 13, 2021, 5:40pm. Values are in % relative to the initial model. The limits of the colorscale X are shown in the lower left corner of each plot.

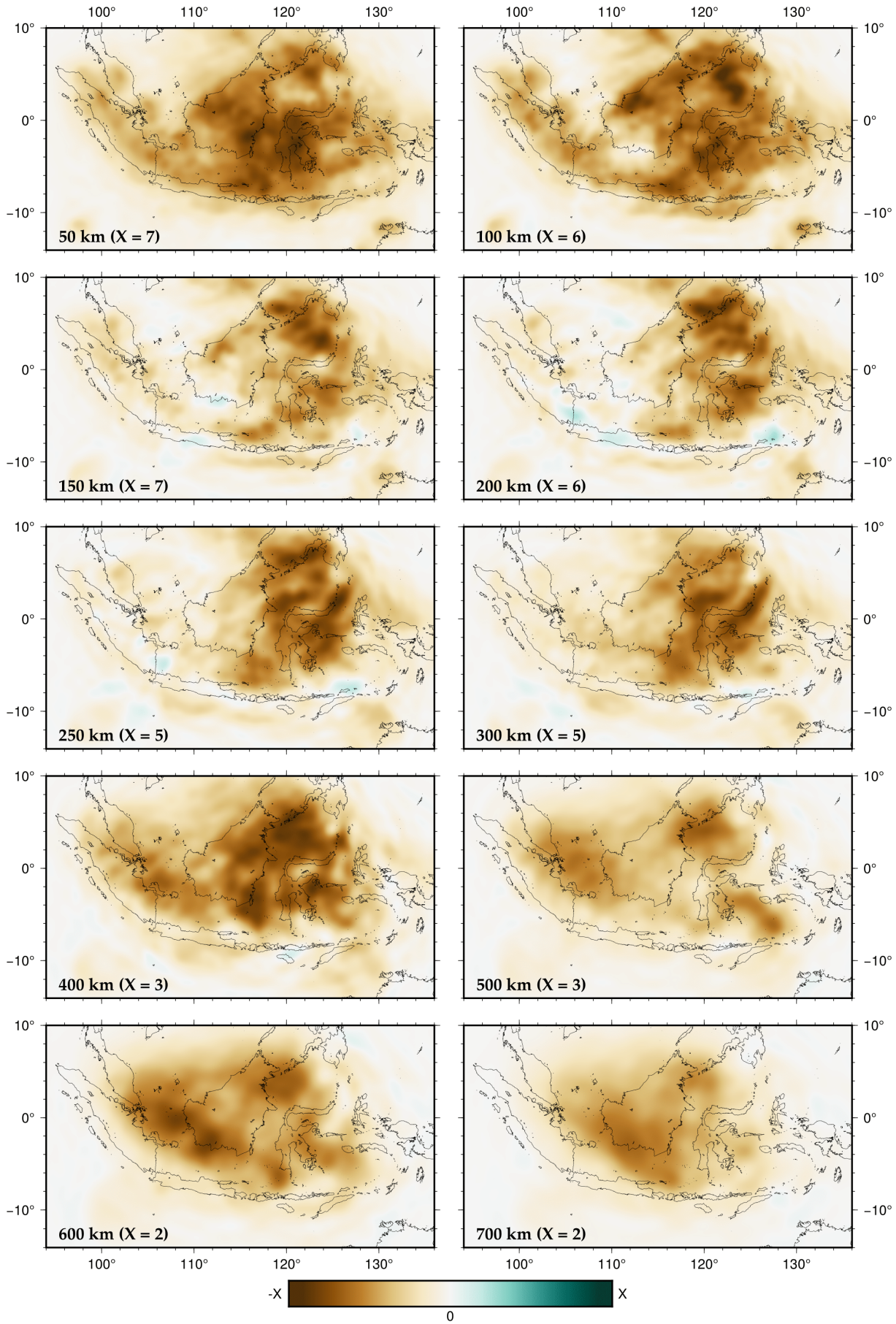

Figure S7c. v_P depth slices from 50 to 700 km. Perturbations are in % relative to the initial model. The limits of the colorscale X are shown in the lower left corner of each plot.

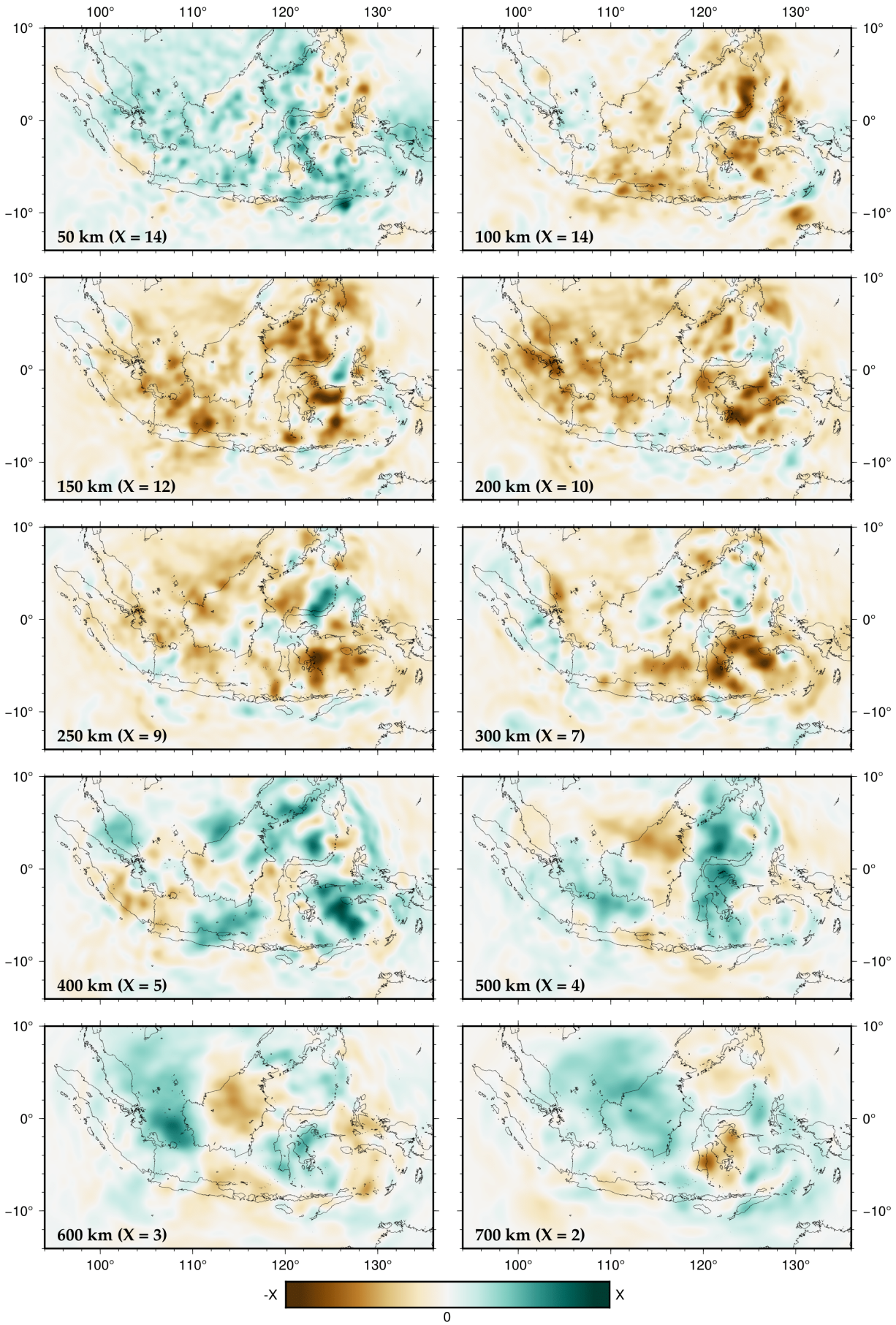

Figure S7d. Density (ρ) depth slices from August 13, 2021, 5:40pm. Perturbations are in % relative to the initial model. The limits of the colorscale X are shown in the lower left corner of each plot.